

# 3D Reconstruction and Visualization of Volume Data in Electrical Capacitance Tomography

Hua Yan

School of Information Science and Engineering, Shenyang University of Technology, Shenyang, China  
Email: yanhua\_01@163.com

Yang Lu and Yifan Wang

School of Information Science and Engineering, Shenyang University of Technology, Shenyang, China  
Email: { yanglusimon6, wyf2001315}@163.com

**Abstract**—Electrical capacitance tomography (ECT) is a non-invasive imaging technique that aims at visualization the permittivity distribution of dielectric materials based on the measured capacitances. In this paper, the 3D finite element models of a direct 3D ECT sensor with or without dielectric spheres inside the sensor are set up by using finite element modeling. The sensitivity analysis of the sensor is carried out by means of electric field intensity. A Landweber iteration method with non-zero threshold is presented to reconstruct 3D permittivity distributions directly. 3D visualization of the reconstructed result (volume data) is achieved by iso-surface. 3D images reconstructed and error analysis show that the Landweber iteration method with non-zero threshold has much better reconstruction performance compared with the classic Landweber iteration method.

**Index Terms**—ECT, 3D reconstruction, 3D visualization, finite element modeling

## I. INTRODUCTION

Electrical capacitance tomography (ECT) is a non-intrusive and non-destructive imaging technique that seeks to image materials with a contrast in dielectric permittivity using measurements of capacitance between a set of electrodes, which are placed around the periphery of a vessel or pipe to be imaged. The 2D or 3D material distribution within the vessel can be obtained from the measured data by a suitable reconstruction algorithm. ECT offers some advantages over other tomography modalities, such as no radiation, rapid response, low construction cost and suitability for small or large vessel. Typical applications of ECT include the monitoring of oil-gas flows in pipelines, gas-solids flows in pneumatic conveying and imaging flames in combustion [1]-[5]

The classic ECT is to reconstruct 2D images of a process cross section. Most processes take place in 3D

space; therefore direct 3D ECT [2]-[4] has gained increased attention in the past few years. As a classic ECT system, a direct 3D ECT system consists of three basic components: a capacitance sensor, a data acquisition system, and an image computer for reconstruction and viewing. The basic structure of the sensor and the measurement concept in direct 3D ECT are the same as in classic ECT. The difference lies in the layout of electrodes. The electrodes are arranged in single-layer for a classic ECT sensor, while a direct 3D ECT sensor usually has at least two-layer electrodes in axial direction.

In ECT technique, the forward problem is to determine the capacitance values for known permittivity distribution. Conversely, the inverse problem is to obtain the material distribution (permittivity) distribution) from the capacitance measurements — a process known as image reconstruction [5]. Currently, the research on direct 3D ECT is still in its initial stage. The reasons for this are serious difficulties in sensor design, measurement circuit design, 3D finite element (FE) modeling, reconstruction algorithms and 3D visualization [4]. In this paper, the authors present their work on direct 3D ECT. 3D FE modeling, 3D sensitivity calculation and analysis, 3D reconstruction algorithm and 3D visualization are focused on.

## II. DIRECT 3D ECT SENSOR AND ITS 3D FE MODELING

### A. The Structure of the Sensor

A direct 3D ECT sensor with 12 electrodes is used in this paper. The 12 electrodes numbered from 1 to 12 are arranged on the outer surface of an insulating pipe in three layers, each layer has four electrodes, as shown in Fig.1. The height, inner and outer diameters of the pipe are 54mm, 46mm and 50mm, respectively. The pipe wall is assumed to have a relative permittivity of 4. The earthed screen is 8mm from the electrode array. Each electrode is 9mm in height and 29.45mm in width. The gap length between electrodes in the horizontal and vertical direction is 9.8mm and 9mm, respectively.

Manuscript received December 10, 2012; revised January 15, 2013; accepted April 12, 2013.

Project numbers: National Natural Science Foundation of China (61071141).

To establish the mathematical model of the sensor, it is necessary to describe how the capacitance measurements are performed. In a complete measurement cycle, an excitation potential  $V_c$  is first supplied to electrode 1 (which is referred to as the source electrode) and the capacitances between 1 and 2, 1 and 3, ..., and 1 and  $L$  ( $L$  is the number of electrodes) are measured. Next, electrode 2 is the source electrode and the capacitances between 2 and 3, 2 and 4, ..., and 2 and  $L$  are measured. This process continues until electrode 11 is the source electrode, and the capacitance between 11 and 12 are measured [5]-[7]. The earthed screen and all the electrodes besides the source electrode are at earth or virtual earth potential in the measurement. In this way, a total of  $M = L(L-1)/2$  independent capacitance measurements are produced in a cycle. In this paper,  $L=12$  and  $M =66$ .

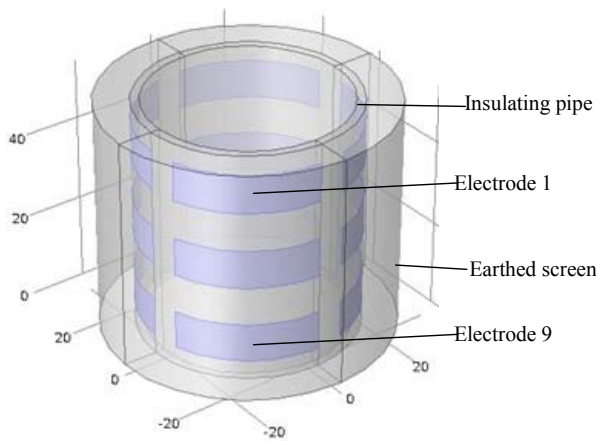


Figure 1. Structure of a direct 3D ECT sensor.

**B. 3D FE Modeling of the Sensor**

The electrostatic field in ECT sensor is governed by Laplace's equation (assuming no free charge inside the screen) [7]-[8]:

$$\nabla \cdot [\varepsilon(x, y, z)\nabla\varphi(x, y, z)]=0 \tag{1}$$

and the associated boundary conditions (the Dirichlet conditions, i.e. the known potentials of all the electrodes and the screen) imposed by the measurement technique, when electrode  $i$  is the source electrode ( $i = 1, 2, \dots, 11$ ), are

$$B = \{(\varphi(\Gamma_i) = V_c) \cup (\varphi(\Gamma_j (j = 1, \dots, L, j \neq i)) = 0) \cup (\varphi(\Gamma_s) = 0)\}$$

where  $\varepsilon(x, y, z)$  and  $\varphi(x, y, z)$  are, respectively, the 3D permittivity and potential distributions;  $\Gamma_1, \Gamma_2, \dots,$  and  $\Gamma_{12}$  represent the spatial location of the 12 electrodes,  $\Gamma_s$  that of the sensor screen.

Since the permittivity distribution is, in general, very

irregular, there is no analytical solution to (1). Therefore, the finite element (FE) method [8]-[11] is used to obtain a numeric solution. The FE analysis and simulation work in this study is carried out with the help of COMSOL Multiphysics software.

COMSOL Multiphysics is a FE analysis software package for various physics and engineering applications, especially coupled phenomena, or multiphysics. It also offers an extensive interface to MATLAB and its toolboxes for a large variety of programming, pre-processing and post-processing possibilities. The COMSOL Multiphysics simulation environment facilitates all the steps in the modeling process – defining your geometry, meshing, specifying your physics, solving, and then visualizing your results.

The modeling steps used in this study can be listed as follows.

- 1) Select Space Dimension>3D.
- 2) Select AC/DC>Electrostatics (es) in the Add physics tree.
- 3) Select Preset Studies>Stationary in the Studies tree.
- 4) Draw the sensor geometries.
- 5) Set electrical properties in the domains.
- 6) Set the boundary conditions, i.e., add electrodes and earthed screen as terminals.
- 7) Generate the unstructured tetrahedral mesh.
- 8) Solve FE equation and obtain the node potential distribution.
- 9) Compute capacitances and the distribution of electric field intensity (when necessary) using the post-processing capabilities in COMSOL.

When the sensor is empty, the simulation model established by conducting above steps from 1 to 6 is shown in Fig.1. The FE mesh obtained after step 7 is shown in Fig.2; the domain is partitioned into 65385 tetrahedrons.

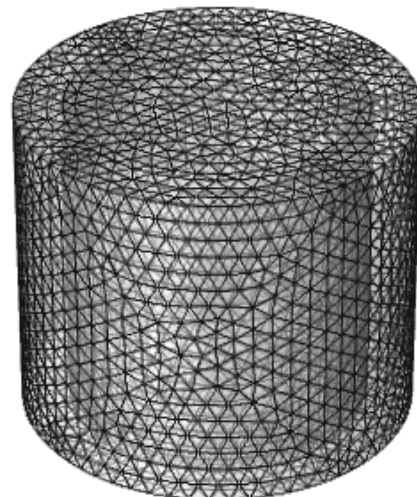


Figure 2. The FE mesh used when the sensor is empty.

**III. 3D SENSITIVITY ANALYSIS**

The sensing field of an ECT sensor is non-uniform distributed in a 3D space. The sensitivity maps are

usually obtained by FE analysis [8]. Subdividing the domain (the volume enclosed by the screen) into a number of voxels (volume element), the sensitivity of  $k$ th voxel of electrode pair  $i$ - $j$  can be defined as:

$$s_{ij}(k) \cong - \int_{V_k} \frac{E_i(x, y, z) \cdot E_j(x, y, z)}{V_c^2} dx dy dz \quad (2)$$

where  $E_i(x, y, z), E_j(x, y, z)$  are the electric field intensity when the excitation voltage  $V_c$  is applied to  $i$ th electrode and  $j$ th electrode, respectively,  $V_k$  denotes the  $k$ th voxel.

FE meshes in 2D tomography usually have a few hundred pixels. In the case of 3D tomography the number of voxels reaches up to thousands or even more. Using a typical FEM mesh generator, the obtained mesh is denser in the vicinity of the electrodes and sparser in the middle. This is desirable since the electric field can be calculated more accurately but, as a result, a lot of elements are very small. From the view of reconstruction point, this is a waste of valuable computing resources and results in more undetermined inverse problem (more elements are used to construct the domain to be reconstructed). In [4], a coarse and homogeneous 3D FE mesh is used for FE analysis and image reconstruction, thus the problem caused by an inhomogeneous distribution of element density is avoided at the cost of FE analysis accuracy.

The values of the electric field intensity required are calculated using the FE mesh shown in Fig.2. But this FE mesh is not used for image reconstruction since it is inhomogeneous, with a lot of very small elements. Another homogeneous mesh is generated specially for image reconstruction. In doing so, the  $46\text{mm} \times 46\text{mm} \times 54\text{mm}$  space is digitized into  $23 \times 23 \times 24$  voxels, each voxel is  $2\text{mm} \times 2\text{mm} \times 2.5\text{mm}$ . In this way, both the requirements of FE analysis and image reconstruction are ensured.

In the mesh for image reconstruction, the layers in  $z$  direction are 24. Layer 1 is in the bottom. Electrode 1~4 occupy layer 19~22, electrode 5~8 occupy layer 11~14, and electrode 9~12 occupy layer 3~6. To illustrate the 3D sensing field of the sensor, two positions in cross-section are selected, one in the center, and the other near the wall, see Fig.3 (a). The normalized sensitivity maps for all 66 electrode pairs corresponding these two positions are given in Fig.3 (b) and (c), which can present the axial distribution of sensitivity more clearly. Following can be found in Fig.3.

- 1) The difference in sensitivities among different electrode pairs is very large;
- 2) The sensitivity inhomogeneity of any electrode pair is very serious.

The sensitivity analysis is necessary for ECT sensor design. Not only that, the sensitivity matrix (Jacobian)  $S$  obtained by sensitivity analysis plays a crucial role in image reconstruction. Currently, LBP method and Landweber iteration method are the most widely used reconstruction algorithms. LBP is simple and fast, but the quality of the image reconstructed by LBP is relatively low. Compare with LBP, Landweber iteration method can

produce much better images at the expense of more time consuming [5],[12]-[13].

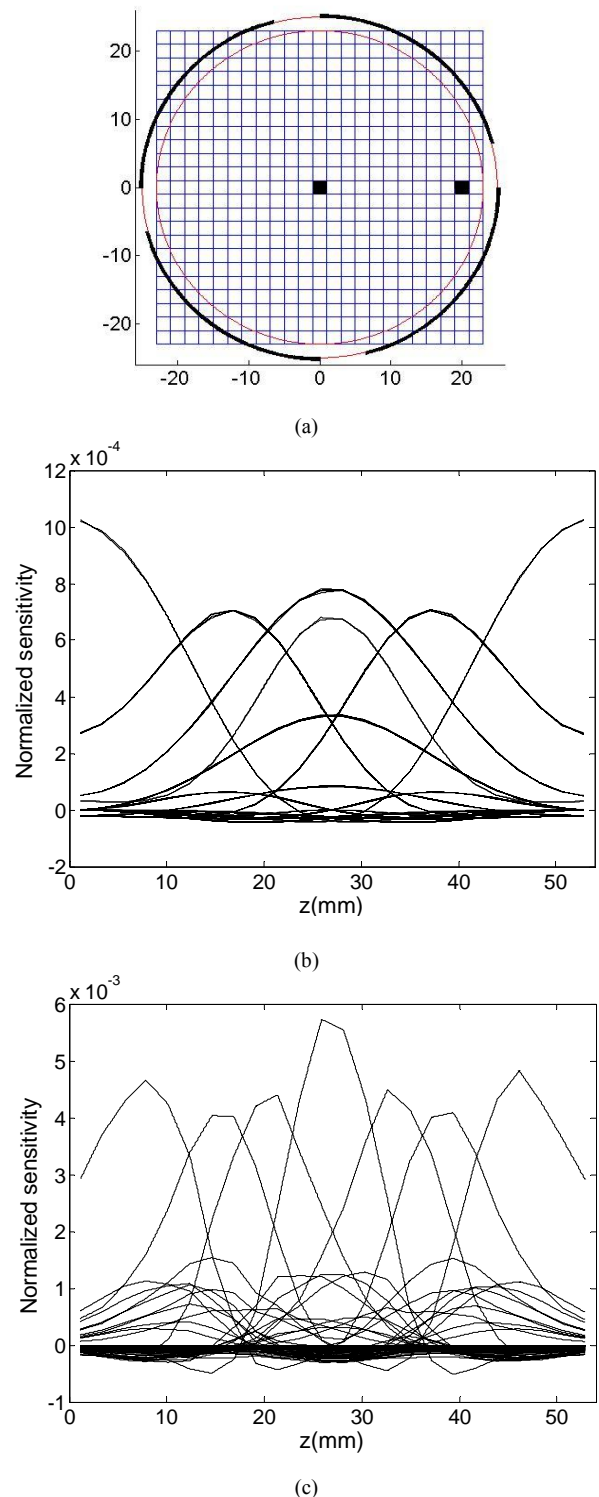


Figure 3. Normalized sensitivity maps for all 66 electrode pairs in selected positions. (a) Two positions selected. (b) Axial sensitivity maps in the center. (c) Axial sensitivity maps near the wall.

#### IV. LANDWEBER ITERATION METHOD WITH NON-ZERO THRESHOLD

### A. Classic Landweber Iteration Method

In ECT, the relationship between the measured capacitance and the permittivity distribution of the region to be reconstructed is nonlinear but, for simplicity, can be simplified to a linear form  $C = SG$ .  $G$ ,  $C$  and  $S$  are the normalized permittivity (i.e. grey level) vector, the normalized capacitance vector and the normalized sensitivity matrix.

The Landweber iteration method is one of the variations of the steepest gradient descent method and its cost function to be minimized is expressed as

$$f(G) = \frac{1}{2} \|C - SG\|^2 \quad (3)$$

The gradient of  $f(G)$  with respect to  $G$  can be defined as

$$\nabla f(G) = S^T(C - SG) \quad (4)$$

The iteration procedure of classic Landweber iterative method can be written as:

$$\begin{aligned} G_{k+1} &= P[G_k + \nabla f(G) = G_k + \alpha S^T(C - SG_k)] \\ P(x) &= \begin{cases} 0 & \text{if } x < 0 \\ x & \text{if } 0 \leq x \leq 1 \\ 1 & \text{if } x > 1 \end{cases} \end{aligned} \quad (5)$$

The non-linear function  $P$  in (5) constrain the reconstructed image so that  $G_{k+1} \in [0,1]$ , i.e. when a normalized grey level is less than zero it is constrained to zero and when it is larger than "1" it is constrained to "1". It has been found that the inclusion of the constraint function is necessary in order to regularize the iteration and to produce a stable solution. Usually, the initial image is obtained by LBP method [12]-[13], and the step length  $\alpha = 2/\lambda_{\max}$ ,  $\lambda_{\max}$  is the maximum eigenvalue of  $S^T S$ .

### B. Landweber Iteration Method with Non-zero Threshold

Classic Landweber iterative method given in (5) usually can reconstruct good images in 2D ECT system. But when using in direct 3D ECT system, its reconstruction images are not satisfactory due to the existence of too many artifacts, see Fig. 4 in section V.

An image artifact is any pattern within an image which is not present within the original object. As seen in (5), the image vector is corrected iteratively by  $\alpha S^T(C - SG_k)$ . When the number of capacitance data is much smaller than the number of pixels,  $(C - SG_k)$  becomes insignificant, and the image is basically corrected by  $S^T$ , producing the so-called "sensitivity-caused artifacts". That is, the generated image seems to be directed toward the stronger sites of the sensitivity. These "sensitivity-caused artifacts" are often found in 2D reconstruction images too, but in 3D reconstruction images, they become much more significant. This is because the

number of pixels is considerably increased and the inhomogeneity of sensing field is more serious.

Unfortunately, function  $P$  can not reduce the "sensitivity-caused artifacts", and these low-level artifacts would be enhanced in iteration. In order to reduce the low-level artifacts timely, we modified (5) as follows.

$$\begin{aligned} G_{k+1} &= p[G_k + \nabla f(G) = G_k + \alpha S^T(C - SG_k)] \\ p(x) &= \begin{cases} 0 & \text{if } x < \eta \\ x & \text{if } \eta \leq x \leq 1, \quad 0 < \eta < 1 \\ 1 & \text{if } x > 1 \end{cases} \end{aligned} \quad (6)$$

That is, we replaced the original zero threshold in (5) with a small positive number  $\eta$ . We call this method as the Landweber iteration method with non-zero threshold. In this paper,  $\eta$  is fixed at 0.04. The reconstruction results given in section V indicate that the non-zero threshold can reduce artifacts effectively.

For convenience, we also call the method described in (5) as classic Landweber, the method described in (6) as Landweber with non-zero threshold.

## V. TEST OF RECONSTRUCTION PERFORMANCE

### A. Test Phantoms

We carried out extensive computer simulation with synthetic data to illustrate the reconstruction performance of Landweber with non-zero threshold. The test object is a dielectric sphere, the radius of the sphere is 4.5mm, and the relative permittivity of the sphere is 2.6. Four test phantoms are generated in COMSOL. Phantom 1, with a sphere located in (0, 0, 27), is partitioned into 67533 tetrahedral. Phantom 2, with a sphere located in (0, 0, 9), is partitioned into 67709 tetrahedrons. Phantom 3, with two spheres located in (0, 0, 9) and (0, 0, 45) respectively, is partitioned into 69843 tetrahedrons. Phantom 4, with a sphere located in (0, 0, 18), is partitioned into 67949 tetrahedrons. The phantoms are given in the first column of Fig.4. The simulation data of the capacitance measurements are calculated in COMSOL.

### B. 3D Visualization of Volume Data

A very important step of the inverse process is to present reconstruction results and show them in a suitable and realistic form. The reconstruction result of 3D ECT is scalar volume data, which comprises four 3D arrays. The  $X$ ,  $Y$ , and  $Z$  arrays specify the coordinates of the scalar values (i.e. the reconstructed normalized permittivities) in the array  $G$ . Volume visualization is the creation of graphical representations of data sets that are defined on 3D grids. The techniques you select to visualize volume data depend on what type of data you have and what you want to learn. In general, scalar data is best viewed with isosurfaces, slice planes, and contour slices. In this paper, isosurfaces are used since they can display the overall structure of a volume.

The information conveyed by a complex 3D graph can be greatly enhanced through careful composition of

the scene. Viewing techniques include adjusting camera position, specifying aspect ratio and project type, zooming in or out, and so on. In addition, lighting is an effective means to enhance the visibility of surface shape and to provide a 3D perspective to volume graphs.

The 3D images given in this paper are isosurface displays with an isovalue of 0. Viewing techniques such as default 3D view, a light right and up from camera and Gouraud lighting are used to generate effective visualizations. The PDF document should be sent as an *open file*, i.e. without any data protection.

C. Evaluation of Errors

In addition to the 3D visualizations of reconstructed results, following three criteria are used in order to evaluate the reconstruction quality quantitatively: spatial image error *SIE*, volumetric error *VE*, and correlation coefficient *CC* [5]-[6], [13].

*SIE* represents the spatial error information as one would see on the difference image. It contains all the spatial errors such as those in shape, position and volume of the reconstructed object. *SIE* is defined as follows:

$$SIE = \frac{\sum_{k=1}^N |G(k) - \hat{G}(k)|}{\sum_{k=1}^N G(k)} \tag{7}$$

$$G(k) = \begin{cases} 1, & \text{if the centroid of the } k\text{th voxel is} \\ & \text{in the high permittivity region} \\ & \text{of the phantom} \\ 0, & \text{otherwise} \end{cases} \tag{8}$$

$$\hat{G}(k) = \begin{cases} 1, & \text{if the grey level of the } k\text{th voxel in the} \\ & \text{reconstructed image is non - zero} \\ 0, & \text{otherwise} \end{cases} \tag{9}$$

*VE* represents the relative volume error between the reconstructed object and the true object. It is defined as follows:

$$VE = \frac{|V_R - V_T|}{V_T} \tag{8}$$

where  $V_T$  and  $V_R$  are the volume of the true object and the reconstructed object, respectively.

*CC* represents the correlation coefficient between the true and reconstructed permittivities. It is defined as follows:

$$CC = \frac{\sum_{k=1}^N (\hat{g}_k - \bar{\hat{g}})(g_k - \bar{g})}{\sqrt{\sum_{k=1}^N (\hat{g}_k - \bar{\hat{g}})^2 \sum_{k=1}^N (g_k - \bar{g})^2}} \tag{9}$$

where  $\hat{g}_k$  and  $g_k$  are, respectively, the reconstructed and real normalized permittivity of the  $k$ th voxel;  $\bar{\hat{g}}$  and  $\bar{g}$

are, respectively, the mean value of the reconstructed and real normalized permittivity vector.

Small *SIE*, *VE* and *CC* closer to 1 give a better reconstruction performance.

D. Reconstruction Results

Both classic Landweber and Landweber with non-zero threshold are used for image reconstruction. The reconstruction results are obtained after 100 iterations. Fig. 4 gives the true objects and the objects reconstructed. Table I gives the reconstruction errors.

Following can be found from Table I and Fig. 4.

1) The objects reconstructed by classic Landweber are much bigger than the true objects, combined with scattered artifacts.

2) The objects reconstructed by Landweber with non-zero threshold are similar to the true objects. No scattered artifacts are found in these 3D isosurfaces.

3) Compare with classic Landweber, Landweber with non-zero threshold can generate much smaller *SIE*, *VE*, and *CC* closer to 1.

VI. CONCLUSIONS AND FURTHER PLAN

In this paper, the 3D reconstruction and visualization techniques in ECT are investigated. A Landweber iteration method with non-zero threshold is presented to reconstruct 3D permittivity distributions directly from the measured capacitances. The 3D visualizations of the volume data obtained are achieved by iso-surfaces. Extensive simulation researches conducted in COMSOL show the following.

1) The Landweber iteration method with non-zero threshold can produce much better 3D images than can the classic Landweber iteration method. The 3D objects reconstructed by Landweber with non-zero threshold are much closer to the true objects, both in shape and in size, than are those reconstructed by classic Landweber.

2) Compare with classic Landweber, Landweber with non-zero threshold can generate much smaller spatial image error, much smaller volume error, and correlation coefficient closer to 1.

3) The use of non-zero threshold can reduce the low-level artifacts effectively and simply.

4) Simulation research on direct 3D ECT can be conducted by means of COMSOL efficiently.

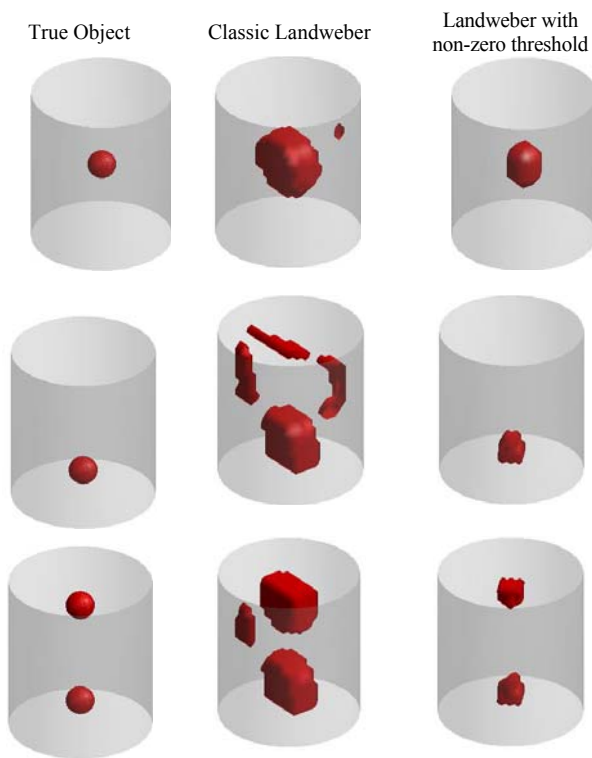
In the current stage of development, the quality and spatial resolution of the images are still insufficient. The selection of the number of voxels is a trade-off. Defining more voxels makes the inverse problem more undetermined, while using of too few voxels results in coarse images. We intend to overcome these issues by increasing the number of electrodes, optimizing the structure and parameters of the sensor, improving the algorithms of reconstruction and visualization, so better quality and spatial resolution could be achieved.

ACKNOWLEDGMENT

This work is supported by National Natural Science Foundation of China (grant no. 61071141).

TABLE I.  
RECONSTRUCTION ERRORS

Phantom	Classic Landweber	Landweber with non-zero threshold
1	$SIE=7.6136$	$SIE=1.3182$
	$VE=7.6136$	$VE=1.3182$
	$CC=0.6234$	$CC=0.7192$
2	$SIE=7.1818$	$SIE=0.2727$
	$VE=7.1818$	$VE=0.0909$
	$CC=0.6586$	$CC=0.8603$
3	$SIE=5.5341$	$SIE=0.4091$
	$VE=5.5341$	$VE=0.2273$
	$CC=0.6606$	$CC=0.7810$
4	$SIE=7.2500$	$SIE=0.9091$
	$VE=7.2500$	$VE=0.7273$
	$CC=0.6335$	$CC=0.8062$



REFERENCES

[1] W. Q. Yang, "Design of electrical capacitance tomography sensors", *Meas. Sci. Technol.*, vol.21, April 2010. doi:10.1088/0957-0233/21/4/042001.  
 [2] W. Warsito, Q. Marashdeh and L. S. Fan, "Electrical Capacitance Volume Tomography", *IEEE Sens. J.*, vol. 7, pp. 525-535, April 2004.  
 [3] F. Wang, Q. Marashdeh, L.S. Fan and W. Warsito, "Electrical Capacitance Volume Tomography: Design and

Applications", *Sensors*, vol.10, pp. 1890-1917, March 2010.  
 [4] R. Wajman, R. Banasiak, L. Mazurkiewicz, T. Dyakowski and D. Sankowski, "Spatial Imaging with 3D Capacitance Measurements", *Meas. Sci. Technol.*, vol.17, pp. 2113-2118, August 2118.  
 [5] H. Yan, L. J. Liu, H. Xu and F. Q. Shao, "Image reconstruction in electrical capacitance tomography using multiple linear regression and regularization", *Meas. Sci. Technol.*, vol.12, pp. 575-581, May 2001.  
 [6] C. G. Xie, S. M. Huang, C. Lenn, A. Stott and M. S. Beck, "Experimental evaluation of capacitance tomographic flow imaging systems using physical models", *IEE Proc. G*, vol. 141, pp. 357-68, October 1994.  
 [7] C. G. Xie, S. M. Huang, B. S. Hoyle, R. Thorn, C. Lenn, D. Snowden and M. S. Beck, "Electrical capacitance tomography for flow imaging: system model for development of image reconstruction algorithms and design of primary sensors", *IEE Proc. G*, vol.139, pp. 89-98, February 1992.  
 [8] H. Yan, F. Q. Shao, H. Xu and S. Wang, "Three-dimensional analysis of electrical capacitance tomography sensing fields", *Meas. Sci. Technol.*, vol.10, pp. 717-725, August 1999.  
 [9] Z. G. Wang, S. P. Peng and T. Liu, "GPU accelerated 2-D staggered-grid finite difference seismic modeling", *Journal of Software*, vol.6, n.8, pp. 1554-1561, 2011.  
 [10] Z. F. Ming, T. Wen and T. Chen, "The simulation of electromagnetic suspension system based on the finite element analysis", *Journal of Computers*, vol. 8. n. 2, pp. 308-312, 2013.  
 [11] R. Banasiak, R. Wajman and D. Sankowski, "Three-dimensional nonlinear inversion of electrical capacitance tomography data using a complete sensor model". *Progress In Electromagnetics Research*, vol. 100, pp. 219-234, 2010.  
 [12] W. Q. Yang, D. M. Spink, T. A. York, H. McCann, "An image-reconstruction algorithm based on Landweber's iteration method for electrical-capacitance tomography", *Meas. Sci. Technol.*, vol. 10, pp. 1065-1069, November 1999.  
 [13] W. Q. Yang and L. H. Peng, "Image reconstruction algorithms for electrical capacitance tomography", *Meas. Sci. Technol.*, vol. 14, pp.1-13, January 2003.

**Hua Yan** was born in Shenyang, China. She received her PhD degree from Northeastern University, China. She is now a professor in School of Information Science and Engineering, Shenyang University of Technology. Her research interests include electrical capacitance tomography, acoustic travel-time tomography, and digital signal processing.

**Yang Lu** was born in Shenyang, China. He is now studying as master student in Shenyang University of Technology. His research interests in electrical capacitance tomography.

**Yifan Wang** was born in Jinzhou, China. He received his master degree from Shenyang University of Technology, China. He is now studying as PhD student in Shenyang University of Technology. His research interests in electrical capacitance tomography.